RESEARCH ARTICLE

ADVANCED MATERIALS INTERFACES Open Access

www.advmatinterfaces.de

Structural Insights Into Aluminum-Doped Manganese Dioxides as Promising Materials for Direct Lithium Extraction: Modeling and Mechanism Study

Shuxuan Yan, Shaozhen Pei, Xiaodong Li, Zhongyan Luo, Xiangping Chen,* Małgorzata Szlachta, and Junhua Xu**

This study aimed to provide new insights into lithium (Li) sorption and extraction mechanisms by systematically investigating the structure, surface properties, and defect vacancies of both doped and undoped manganese oxide sorbents. HMnO and Al-doped HMnO sorbents are successfully synthesized, and their formulas and vacancy ratios are determined using X-ray diffraction (XRD), Fourier transform infrared spectroscopy (FTIR), Raman spectroscopy, thermal gravimetric analysis (TGA), X-ray photoelectron spectroscopy (XPS), and inductively coupled plasma-atomic emission spectroscopy (ICP-AES) characterization. Among the materials tested, HMO-2.5Al exhibited the best performance in batch sorption experiments, enhancing Li^+ sorption to 44.49 mg g^{-1} and reducing Mn loss to 3.38%. HMO-2.5Al also demonstrated exceptional lithium selectivity in the simulated brine test, with separation factors of α^{Li}_{Ca}, α^{Li}_{Na}, α^{Li}_{K} and α^{Li}_{Mg} being 3.33, 353.08, 1327.44, and 6552.76, respectively. The sorbent displayed sustained durability before and after five cycles of sorption-desorption. The ion exchange-surface complexation model is employed to investigate the titration behavior, pH effects, and sorption isotherms, providing insights into the mechanism underlying Li^+ sorption. A two-stage sorption mechanism is proposed, involving a surface ion exchange reaction and a surface complexation reaction. Overall, the synthesized HMO-2.5Al sorbents demonstrate significant potential for direct lithium extraction from solutions with high concentrations of coexisting ions and contribute a novel mechanism to the field of lithium extraction study.

1. Introduction

Lithium is the lightest metal element and has a wide range of applications in various fields, including lithium-ion batteries, nuclear power, and aerospace materials.[1,2] Lithium resources are commonly found in brines, seawater, clays, and ores.[3] Previous studies on the global geographic distribution of lithium resources have reported that 61.8% of verified lithium resources exist in brines and 25% in minerals.[3] Lithium extraction from salt lakes, geothermal brines, and seawater has increasingly emerged as a vital source of lithium due to their abundance. However, the extraction process from such complex brines often involves high concentrations of coexisting ions, including sodium, potassium, magnesium, and calcium, which present significant challenges to the industrialization of lithium-selective recovery processes.

Recently, lithium extraction from aqueous resources has been investigated using numerous techniques, such as precipitation,[4–6] solvent extraction,[7,8] membrane separation,[9] and sorption.[10,11] However, the development of feasible and environmentally sustainable extraction methods from brines remains a significant challenge. Among the emerging techniques, direct lithium extraction (DLE) is notable for its practical and environmental benefits. In contrast to conventional methods using evaporative techniques, DLE enhances both lithium recovery rates and purity while

S. Yan
Hunan Provincial Key Laboratory of Chemical Power Sources
College of Chemistry and Chemical Engineering
Central South University
Changsha 410083, P. R. China

The ORCID identification number(s) for the author(s) of this article can be found under https://doi.org/10.1002/admi.202400912

DOI: 10.1002/admi.202400912

S. Pei, Z. Luo, J. Xu
Nuclear Chemistry & Separation and Purification Technology Laboratory
Fujian Institute of Research on the Structure of Matter
Chinese Academy of Sciences
Fuzhou, Fujian 350002, China
E-mail: junhua.xu@gtk.fi

S. Pei, Z. Luo
College of Chemistry and Materials Science
Fujian Normal University
Fuzhou, Fujian 350007, China

requiring fewer chemical reagents.[12] Inorganic ion exchangers used in DLE are recognized as promising sorbents for lithium sorption and purification due to their high selectivity, stability at elevated temperatures, and resistance to ionizing radiation.[13–15] Manganese-based ion sieves are more attractive adsorbents because of their high selectivity, high recovery, low cost, and rapid sorption rates.[1] Manganese ion sieves have a unique spinel cubic crystal structure and 3D mesh channels with structural stability during the sorption and desorption of $Li.^{+}$[16] For example, $LiMn_2O_4$,[17,18] $Li_4Mn_5O_{12}$,[19,20] and $Li_{1.6}Mn_{1.6}O_4$[21,22] are the most commonly used manganese-based ion sieves. However, in the process of lithium extraction, manganese has been found to gradually dissolve into a solution, which may significantly reduce the Li^+ sorption capacity of manganese oxide compounds after several applied cycles.[23–25]

In order to overcome this problem, doping strategies have been applied to manganese-based ion sieves, because exogenous ions can increase the average chemical valence of Mn in an LMO spinel, thus reducing the Mn^{3+} content, inhibiting the Jahn–Teller effect, or enhancing the octahedral chemical bonding.[26] Qian et al.[27,28] doped Fe^{3+}, Co^{2+}, and Al^{3+} into $Li_{1.6}Mn_{1.6}O_4$, which increased the Li sorption capacity from 32.3 mg g^{-1} to 35.3, 35.4, and 40.9 mg g^{-1}, respectively, with the Mn dissolution reduced from 5.4% to 3.95%, 4.42%, and 2.1%. Chen et al.[29] synthesized Al-doped $LiAl_xMn_{2-x}O_4$ using a hydrothermal method, achieving a sorption capacity of 26.38 mg g^{-1} for the doped sorbent compared to 31.7 m g^{-1} for the undoped sorbent. In terms of dissolution loss, Mn dissolution in the lithium-containing solution was 2.75% for the doped sorbent and 5.53% for the undoped sorbent. Wang et al.[16] synthesized zirconium-coated $Li_{1.6}Mn_{1.6}O_4$ using a solid-phase combustion method, achieving a sorption capacity of 25.96 mg g^{-1} compared to 28.88 mg g^{-1} for the undoped material. The Mn dissolution loss was 0.349% for the zirconium-coated sorbent, significantly lower than the 0.89% observed for the undoped one. Gao et al.[30] synthesized magnetically recoverable iron-doped lithium-ion sieve $LiMn_{2-x}Fe_xO_4$ using a solid-phase method, with the sorption capacity of the undoped HMO during the sorption–desorption cycle ranging from 34.8 to 17.5 mg g^{-1}, and the doped sorption capacity ranging from 30.8 to 20.5 mg g^{-1}, while the dissolution loss of Mn decreased from 2.48% to 0.51% after doping.

Recent studies have increasingly focused on understanding the extraction mechanisms of manganese oxide-based sorbents in the lithium extraction process. Hunter et al.[31] proposed a redox mechanism, suggesting that Mn^{3+} undergoes disproportionation into Mn^{2+} and Mn^{4+} during the extraction process. In this process, Mn^{4+} remains within the spinel structure, forming λ-MnO_2 and preserving the crystal lattice, while Mn^{2+} dissolves in the solution. Shen et al.,[32] on the other hand, proposed an ion exchange mechanism, whereby Li^+ and H^+ ions are exchanged on the ion sieve sorbents. In addition, the formation of oxygen vacancies in manganese oxides during synthesis is often unavoidable.[33] These vacancies, especially after metal doping, can significantly influence the extraction mechanism. Understanding how these vacancies affect the lithium extraction process is a promising area for future research. To this end, further investigations integrating synthesis, sorption experiments, and modeling will be essential in elucidating the underlying mechanism. In this study, sorbent synthesis, batch sorption experiments, and model development were integrated to explore the mechanism of Li sorption and extraction. First, $Li_{1.6}Mn_{1.6}O_4$ and Li, Al co-doped $Li_{1.6}Mn_{1.6}O_4$ were prepared using a hydrothermal reaction calcination method, and second, the effects of different Li, Al doping contents on the phase composition, dissolution loss, and sorption properties were systematically investigated to determine the optimal preparation and sorption conditions. Furthermore, a series of batch sorption experiments were systematically carried out to investigate the sorption performance and properties of Li, Al co-doped $Li_{1.6}Mn_{1.6}O_4$. The lithium-ion sorption selectivity and cycling performance were tested in a simulated brine solution. Additionally, a sorption-surface complexation model was developed, utilizing a coupling technique that integrated PHREEQC with Python for in-depth analysis of titration, pH effects, and sorption isotherms. Finally, a novel mechanism was proposed for Li^+ sorption and extraction by synthesized Li, Al co-doped $Li_{1.6}Mn_{1.6}O_4$.

2. Results and Discussion

2.1. Structural Analysis

The crystal structures of synthesized LMO and Al-doped LMO were analyzed by XRD (**Figure 1**). The XRD patterns of the materials indicated that the crystal structure was identical to that of orthorhombic $LiMnO_2$ (JCPDS NO. 35–0749; Figure 1a). The XRD patterns of different LMO and Al-doped LMO powders are displayed in Figure 1b. The main diffraction peaks of the samples were 18.80°, 36.56°, 38.27°, 44.53°, 48.68°, 58.93°, 64.68°, and 68.03°, corresponding to eight crystal planes of (111), (311), (222), (400), (331), (511), (440), and (531), respectively. The sharp diffraction peaks indicate good crystallinity, which is indexed to the spinel structure of $Li_{1.6}Mn_{1.6}O_4$ and a face-centered cubic system (Fd-3m) (JCPDS NO.52-1841). The distinct diffraction peaks of the synthesized materials indicate that $Li_{1.6}Mn_{1.6}O_4$ possesses high crystallinity. A slight shift in the diffraction peak positions of (111), (400), and (410) toward higher 2θ values was observed in LMO-10Al, with a higher Al content. This shift can be attributed to the partial substitution of Al^{3+}, whose ionic radius (0.61 Å) is smaller than that of Mn^{3+} (0.66 Å) and Mn^{4+} (0.62 Å)[29,34] Furthermore, as illustrated in Figure S1 (Supporting Information), there was a gradual decrease in the lattice constant with an increase in the Al doping content, which confirmed that the peak

X. Li
Department of Chemistry-Radiochemistry
University of Helsinki
P.O. Box 55, Helsinki FI-00014, Finland
E-mail: Xiaodong.Li@helsinki.fi
X. Chen
College of Chemistry and Chemical Engineering
Hunan Normal University
Changsha 410081, P. R. China
E-mail: xiangping_chen@hunnu.edu.cn
M. Szlachta, J. Xu
Geological Survey of Finland
P.O. Box 96, Espoo FI-02151, Finland
M. Szlachta
Faculty of Engineering and Natural Sciences
Tampere University
P.O. Box 541, Tampere FI-33104, Finland

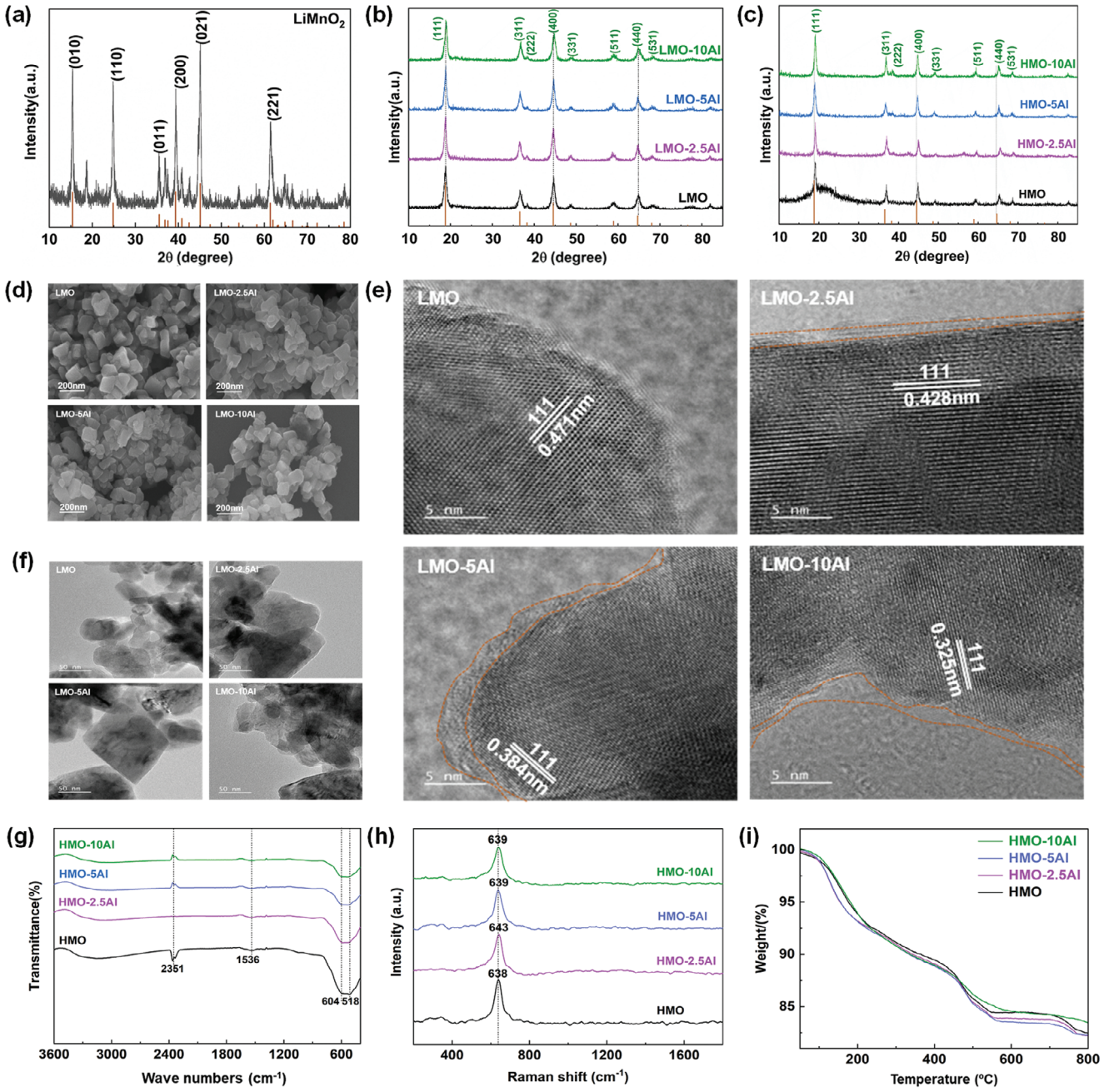

Figure 1. XRD patterns of the obtained materials: a) $LiMnO_2$ and b) LMO, LMO-2.5Al, LMO-5Al, and LMO-10Al; c) HMO, HMO-2.5Al, HMO-5Al, and HMO-10Al; d, e, f) SEM and TEM images of LMO and LMO-Al; g) FTIR spectra of H-type HMO and HMO-Al; h) Raman spectra of H-type HMO and HMO-Al; i) TG-DTA curves of H-type HMO and HMO-Al.

position is slightly shifted to higher 2θ values after doping. The H-type HMO and Al-doped HMO were obtained by acid pickling with 0.1 M HNO_3. Their XRD patterns were consistent with those of LMO and Al-doped LMO, except for a slight shift in the (440) peaks, which may be due to the replacement of Li by H in the structure. The morphologies of LMO and Al-doped LMO samples are presented in Figure 1d–f. The prepared LMO nanoparticles were aggregated as microspheres with a diameter of ≈200 nm (Figure 1e). Figure 1d displays field emission transmission electron microscopy (FESEM) images of Al-doped LMO, revealing that it retained the structural integrity of the microspheres without noticeable distortion. The elemental mapping of O, Mn, and Al in the LMO-2.5Al sample demonstrated an even distribution (Figure S2a, Supporting Information). While the doped adsorbent exhibited a morphology similar to that of LMO, the particle size of the aggregated microspheres decreased as the amount of doped Al increased. Energy-dispersive X-ray spectroscopy (EDS) revealed that the distribution of Al increases as a function of the amount of Al doping (Figure S2b–d, Supporting Information). As illustrated in Figures 1e–f, the outer surface of Al-doped

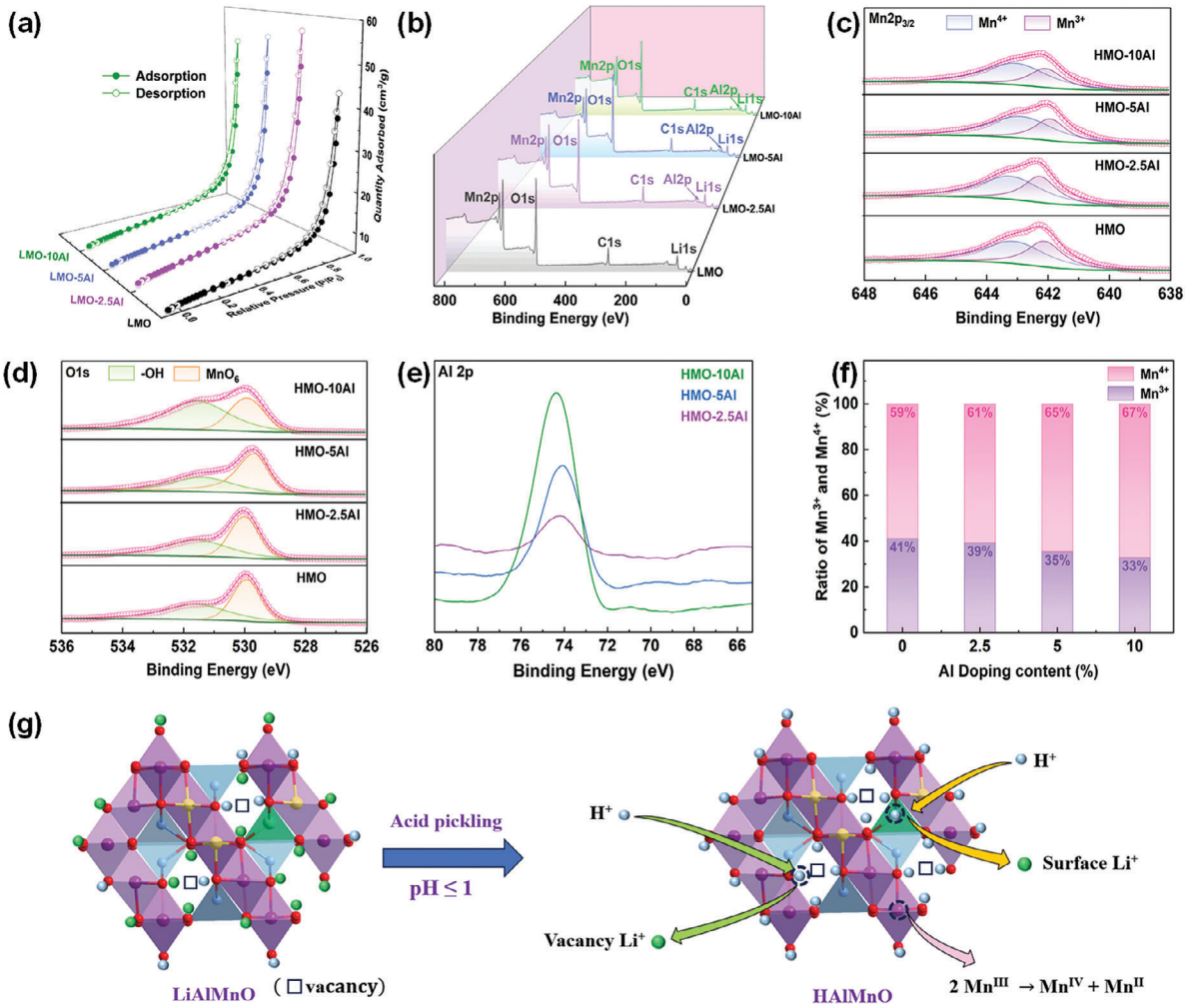

Figure 2. a) Nitrogen sorption–desorption isotherm of LMO and LMO-Al; XPS spectra of the synthesized LMO and LMO-Al: b) full XPS spectra, c) Mn XPS spectra, and d) O1s spectra of H-type HMO and HMO-Al; e) Al 2p of HMO-Al spectra; f) Change in the ratio of Mn^{3+} to Mn^{4+}; g) The proposed mechanism of acid pickling between Al-doped LMO and Al-doped HMO.

LMO is covered by an amorphous layer, indicated by the yellow line. The thickness of this layer is ≈2–3 nm, which indicates that the surface of Al-doped LMO had been successfully coated with a metal oxide layer. This coating is very thin and consists of a monolayer, which can provide an effective protective layer for the spinel particles. The high resolution scanning electron microscopy (HRTEM) images reveal the existence of similar lattice stripes on the surface of and inside LMO and Al-doped LMO. The metal oxide layer can inhibit the dissolution of manganese by preventing the direct contact of lithium-manganese oxides with the pickling solution.[35] The HRTEM images display distinct dot pattern streaks. The (111) intergranular surface of the space group Fd-3m of LMO (0.470 nm) is larger than that of LMO-Al (0.428, 0.384, 0.325 nm), which is consistent with the results of the lattice constants in Figure 1c.

Figure 1g displays the FTIR patterns of HMO and Al-doped HMO. The peaks at 2351 cm^{-1} indicate the stretching vibration of CO_3^{2-}, which might be due to the measurement process being conducted in air, resulting in exposure to CO_2.[36] The peaks at 1536 cm^{-1} are suggested to be the O–H band in HMO, HMO-2.5Al, HMO-5Al, and HMO-10Al.[10,37] The peak at 870 cm^{-1} is ascribed to the Li–O band.[27] The peaks at 518 cm^{-1} result from the Mn(III)-O band and the peaks at 604 cm^{-1} result from the Mn(IV)-O band of [MnO_6] groups.[38,39] With an increase in the amount of Al doping, the peaks shift toward the right. It is notable that the intensity of the Mn(III)-O band increased, while that of the Mn(IV)-O band decreased. This phenomenon indicates that the proportion of Mn(VI) increases and the proportion of Mn(III) decreases with an increase in the amount of Al doping. In addition, Raman spectroscopy was performed for the synthesized materials and is presented in Figure 1h. The synthesized HMO and Al-doped HMO exhibited high wavenumber (608 to 640 cm^{-1}) Raman bands attributed to Mn–O stretching vibrations.[40] Thus, the confirmation of [MnO_6] groups before and after Al doping implies the excellent stability of the [MnO_6] octahedron,[41] which is consistent with the XRD results (**Figure 2b**).

To better understand the thermal stability of the synthesized HMO, HMO-2.5Al, HMO-5Al, and HMO-10Al, TGA was conducted. As illustrated in Figure 1i, the TG curves of the

synthesized materials displayed endothermic peaks with weight loss in the range of 139 to 164 °C (Figure S3a–d, Supporting Information), corresponding to the evaporation of absorbed water.[42] The exothermic peaks with weight loss in the range of 285 to 361 °C can be ascribed to the evaporation of hydroxyl groups with the transformation from spinel to β-MnO_2.[10] The large endothermic peak with weight loss in the range of 478 to 497 °C was due to the transformation from β-MnO_2 to the more stable α-Mn_2O_3 phase, accompanied by the dissipation of oxygen gas.[10] When the temperature reached 800 °C, Mn_2O_3 transformed to MnO, with another stage of weight loss occurring.[43]

The surface properties of the synthesized LMO and Al-doped LMO were evaluated through Brunauer-Emmett-Teller (BET) and XPS analysis. The specific surface area and pore size of the synthesized LMO, LMO-2.5Al, LMO-5Al, and LMO-10Al were analyzed from the N_2 sorption isotherm in Figures 2a and S4a–d (Supporting Information). The sorption curves were of type III in the isotherm classification by Brunauer, which is equivalent to a single multilayer reversible sorption process occurring on nonporous or microporous solids.[44,45] Among the four materials, LMO-2.5Al possessed the highest specific surface area of 17.21 $m^2\ g^{-1}$ and a total pore volume of 0.052 $cm^3\ g^{-1}$. In theory, LMO-2.5Al has more sorption sites than the other synthesized materials, suggesting a higher lithium sorption capacity (Table S1, Supporting Information).

The XPS full spectra of LMO and Al-doped LMO are presented in Figure 2b. The characteristic peaks of the elements C, O, Mn, Al, and Li appeared in the range of 835–0 eV. The main binding energies of Mn2p, O1s, and Al2p at 642.2–643.1, 73.9, and 53.5 eV are ascribed to Mn^{3+}/Mn^{4+}, Al^{3+}, and Li^+, respectively (Figure 2b–d).[46,47] The Al2p peaks were observed in the range of 72–76 eV in the Al-doped LMO samples (Figure 2e). The peak intensity increased with an increase in Al doping, indicating an increase in the Al content on the adsorbent surface. In addition, the proportion of Mn^{4+} increased with an increase in the amount of Al doping (Figure 2f; Table S2, Supporting Information). The suggested reason is that Mn was replaced by Al at 16d sites in the HMO cubic structure, thereby increasing the average valence of Mn.[27] The ratio of Mn^{4+}/Mn^{3+} increased with an increase in the amount of Al doping, which can effectively reduce the dissolution of Mn from HMO-Al. However, excessive Al doping may modify the lattice constant, resulting in the disordering of cations in the crystal structure and aggravating the dissolution loss of Mn.[48] Thus, increasing Al doping to an optimal level raises the concentration of -OH groups, thereby providing additional sorption sites.

Based on the XPS data, XRD, Raman spectroscopy, FTIR, and microwave digestion results, as well as the defection and vacancy concept,[43,49,50] the formulas of the Li-type synthesized sorbents, namely LMO, LMO-2.5Al, LMO-5Al, and LMO-10Al, were calculated and are presented in Table S3 (Supporting Information), and the formulas of HMO, HMO-2.5Al, HMO-5Al and HMO-10Al were calculated and are presented in **Table 1**. Their corresponding H-type sorbents were obtained by acid pickling using 0.1 M HNO_3 (Figure S5a, Supporting Information). After acid pickling, the XPS results for the obtained H-type sorbents indicated that the ratio of -OH increased (Table S4, Supporting Information) compared with that of the pristine Li-type synthesized sorbents (Table S2, Supporting Information). These findings were consistent with the ion exchange reaction, which is in line with Eq. 1from the reference,[32]

Table 1. The calculated chemical formula with vacancy (□) of synthesized H-type sorbents.

Samples	Chemical formula
HMO	$Li_{0.035}\ H_{1.563}\ (Mn(III)_{0.412}Mn(IV)_{0.5885})_{1.652}$ $\square_{0.474}O_4.0.23H_2O$
HMO-2.5Al	$Li_{0.010}H_{1.588}\ Al_{0.01}(Mn(III)_{0.393}Mn(IV)_{0.607})_{1.494}$ $\square_{0.983}O_4.0.22H_2O$
HMO-5Al	$Li_{0.012}\ H_{1.588}\ Al_{0.052}(Mn(III)_{0.344}Mn(IV)_{0.656})_{1.534}$ $\square_{0.636}O_4.0.22H_2O$
HMO-10Al	$Li_{0.002}H_{1.600}\ Al_{0.087}(Mn(III)_{0.329}Mn(IV)_{0.671})_{1.436}$ $\square_{0.865}O_4.0.23H_2O$

$$(Li)\left[Mn^{III}Mn^{IV}\right]O_4 + H^+ \rightarrow (H)\left[Mn^{III}Mn^{IV}\right]O_4 + Li^+ \quad (1)$$

There is an assumption that can be applied to interpret the Mn loss during acid pickling. According to crystal field theory, both high-spin trivalent manganese (Mn^{3+}) and low-spin tetravalent manganese (Mn^{4+}) reside in an octahedral field within an oxygen framework, exhibiting d^4 and d^3 electronic configurations, respectively.[51] The three d electrons of Mn^{4+} occupy stable orbitals, while Mn^{3+} contains an additional, more reactive electron that tends to be lost. As a result, during acid pickling, the average valence of manganese in pristine LiMnO or Al-doped LiMnO sorbent tends to increase. The Li-Mn(III)-O structure becomes unstable, causing Mn^{3+} to release an electron, which migrates to the inner structure and is captured by Mn^{4+}. This process ultimately leads to the formation of Mn^{2+} when Mn^{4+} captures a sufficient number of electrons (Equations 2 and 3):

$$Mn\,(III) - O - Li + 2H^+ \rightarrow Mn\,(IV) + Li^+ + e^- + H_2O \quad (2)$$

$$2Mn\,(IV) + 2e^- \rightarrow Mn\,(II) \quad (3)$$

The dissolution of Mn was confirmed and quantified using the ICP data, as displayed in Figure S5b (Supporting Information). After acid pickling, the Mn^{4+}: Mn^{3+} ratio increased, consistently with Equation (2). In summary, the proposed mechanism of acid pickling of LMO and Al-doped LMO is illustrated in Figure 2g.

2.2. Batch Sorption Experiments

2.2.1. Potentiometric Titration

Potentiometric titration of the synthesized HMO, HMO-2.5Al, HMO-5Al, and HMO-10Al was investigated in a 1.0 M $LiNO_3$ background solution, which was used to sharpen any equivalence points in weakly acidic ion exchangers due to the shift in the equilibrium:

$$ROH + Li^+ \Leftrightarrow R - OLi + H^+ \quad (4)$$

Based on Equation (4), the whole conversion values to the Li form of HMO, HMO-2.5Al, HMO-5Al, and HMO-10Al materials

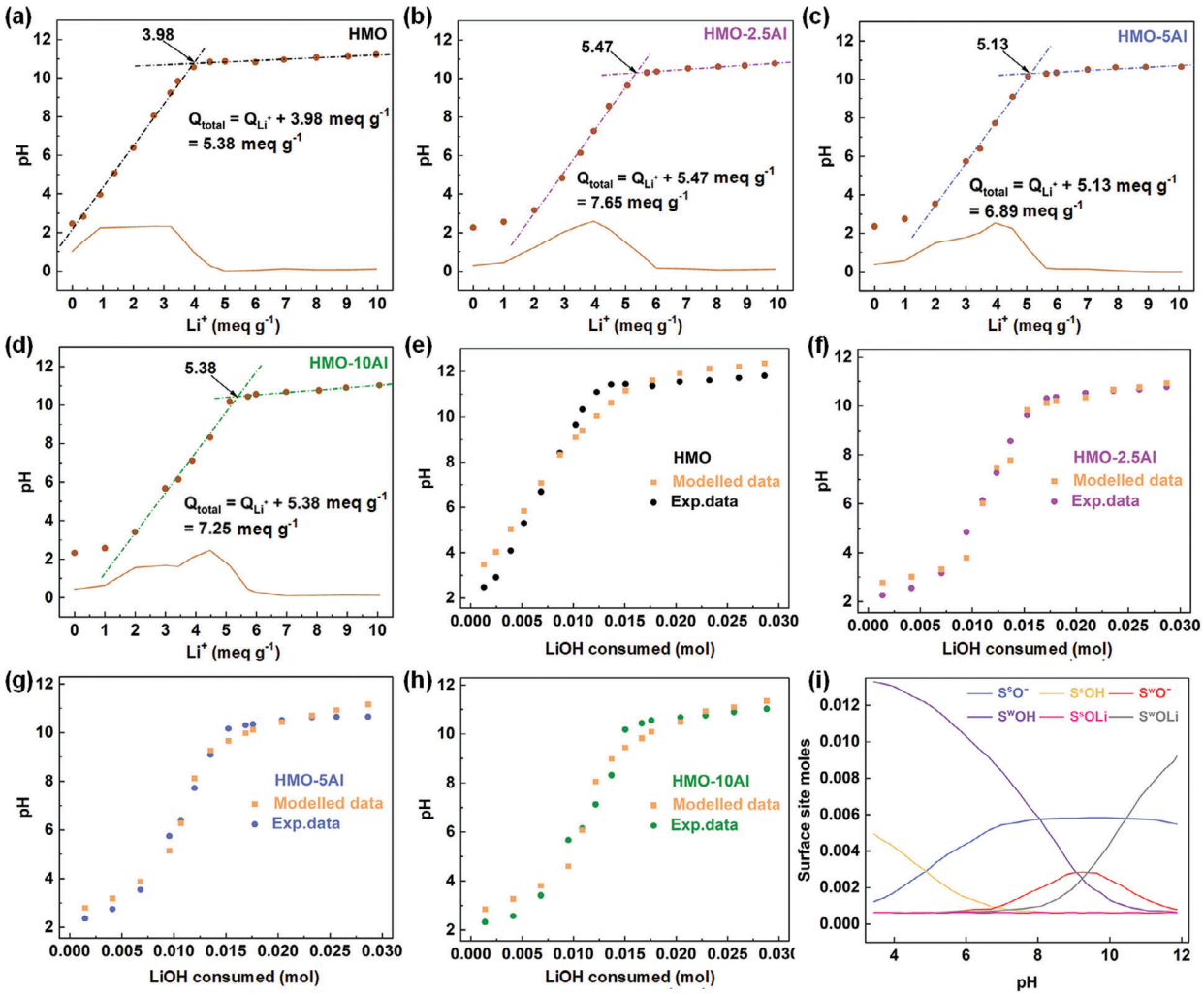

Figure 3. Titration experimental data for Li^+ sorption in a 1 M $LiNO_3$ solution: a) HMO, b) HMO-2.5 Al, c) HMO-5Al, and d) HMO-10Al; Modeling results for titration experimental data: e) HMO, f) HMO-2.5Al, g) HMO-5Al, and h) HMO-10Al; i) The modeled moles of sorption sites on the surface of HMO-2.5 Al.

in the $LiNO_3$ solution were calculated as 1.40, 2.18, 1.76, and 1.87 meq g^{-1}, respectively (**Figure 3**a–d). After titration with LiOH, the ion exchange sites in the material will be balanced by Li^+ ions. The ion exchange capacity can be estimated from the plateau of the curve: 3.98 meq g^{-1} for HMO, 5.47 meq g^{-1} for HMO-2.5Al, 5.13 meq g^{-1} for HMO-5Al, and 5.38 meq g^{-1} for HMO-10Al. The above-obtained capacity values are close to the inflection points of the corresponding MnO_2 presented by the first derivative. Thus, the total cation exchange capacity (CEC) was calculated as 5.38 meq g^{-1} for HMO, 7.65 meq g^{-1} for HMO-2.5Al, 6.89 meq g^{-1} for HMO-5Al, and 7.25 meq g^{-1} for HMO-10Al.

To further illustrate the titration results and surface properties of the synthesized materials, the titration results were modeled based on the protonation/deprotonation reactions and ion-exchange reactions between surface and aqueous Li^+, which were assumed to occur on two surface sites (≡S^SOH and ≡S^WOH): protonation reactions:

$$\equiv SOH + H+ \Leftrightarrow \equiv SOH_2^+ \quad (5)$$

deprotonation reactions:

$$\equiv SOH \Leftrightarrow \equiv SO^- + H^+ \quad (6)$$

and ion-exchange reactions:

$$\equiv SOH + Li+ \Leftrightarrow \equiv SOLi + H^+ \quad (7)$$

The defined surface reactions and their corresponding equilibrium constant values are summarized in **Table 2**. For each type of sorption site, the protonation, deprotonation, and reactions with Li^+ were considered in the titration modeling processes. Table 2 provides the general parameters used for the modeling studies. These primary parameters were fixed for the whole modeling procedure.

The modeled reaction constants (Equations (6) and (7)) for the strong and weak sorption sites are presented in **Table 3** and the results are displayed in Figure 3e–h with experimental data for comparison. The figures illustrate that the modeling results

Table 2. The parameters used in titration and sorption data modeling.

Sample	CEC (meq g^{-1})	Surface area (m^2 g^{-1})	Density of strong sites (sites nm^{-2})	Density of all sites (sites nm^{-2})
HMO	5.38	12.53	99.8	249.2
HMO-2.5Al	7.65	17.21	77.5	191.4
HMO-5Al	6.89	14.52	112.0	217.9
HMO-10Al	7.25	15.63	95.5	208.0

provided a good fit to the experimental results for HMO and Al-doped HMO samples. Figure 3i presents the distributions of different functional groups on the surfaces of HMO and Al-doped HMO samples under different pH conditions. For the four synthesized materials, $\equiv S^SOH$, $\equiv S^WOH$, $\equiv S^SO^-$, $\equiv S^WOH_2^+$, and $\equiv S^WOH$, were found to be the main functional groups, which is in line with Equations (5), (6), and (7). Specifically, at low pH values, the main sorption sites are $\equiv S^WOH$ and $\equiv S^SOH$. At a pH of ≈7 to 8, $\equiv S^SO^-$ becomes the main sorption site. At higher pH levels, $\equiv S^WOLi$ becomes the main sorption site because of the addition of LiOH for pH adjustment. The number of $\equiv S^SO^-$ sites remains constant in both neutral and alkaline conditions, which illustrates the differing behaviors of $\equiv S^WOH$ and $\equiv S^SOH$ sites under different pH conditions.

2.2.2. Effect of pH on sorption

Investigations into the effect of solution pH on Li sorption were performed in a 150 mg L^{-1} $LiNO_3$ solution in a pH range from 4–12. The Li^+ sorption of HMO, HMO-2.5Al, HMO-5Al, and HMO-10Al is illustrated in **Figure** 4a. The overall trend is that the Li^+ sorption of the four synthesized materials increased with an increase in pH. To some degree, the results regarding the pH effect on Li sorption are consistent with the concentration of H^+ ions constraining the ion exchange process. That is to say, the sorption of Li^+ in a high pH solution is favorable. The maximum Li^+ uptake of HMO, HMO-2.5Al, HMO-5Al, and HMO-10Al was 30.95, 34.54, 33.70, and 28.14 mg g^{-1}, respectively, at pH 12 (Figure 4a). In addition, HMO-2.5Al and HMO-5Al displayed the best removal rate of ≈58% (Figure S6, Supporting Information), and the best K_d value was recorded at pH 12 due to the highest amount of Li sorption (Figure 4b).

The effect of pH was modeled according to the assumed surface complexation and ion exchange reactions listed in Table 3. The modeled pH curve provides a good fit to the experimental data (Figure 4c–f). At pH ≤ 11, $\equiv S^SOH_2^+$ and $\equiv S^SOH$ are the main sorption sites, and the surface reactions are dominated by the following ion-exchange equations between Li^+ and surface H^+:

$$Li^+ + \equiv S^SOH_2^+ \Leftrightarrow \equiv S^SOHLi^+ + H^+ \quad (8)$$

$$\equiv S^SOH + Li^+ \Leftrightarrow \equiv S^SOLi + H^+ \quad (9)$$

At pH >11, because of the pH increase, $\equiv S^WO^-$ is the main sorption site, and the surface reaction is dominated by the following surface complexation reaction between Li^+ and $\equiv S^WO^-$:

$$Li^+ + \equiv S^WO^- \Leftrightarrow \equiv S^WOLi \quad (10)$$

The assumption of two sorption sites is based on the structural characteristics of LMO-type materials, which suggest the presence of at least two distinct physical sorption sites: plane and edge surface sites (S) and vacancies (W) within the structural framework. The modeling results indicate that the surface sites (S) more easily sorb Li under low pH conditions. Typically, the surface ion-exchange sites will be occupied first at a low pH. On the contrary, below pH 10, Li migrates with difficulty into material vacancies. The sorption capacity of Al-doped HMO sorbents was observed to follow the order HMO-5Al > HMO-2.5Al > HMO > HMO-10Al. This assumption was further confirmed by the modeled moles of adsorbed species on the surface of HMO from pH 4–12. Surface sites were gradually occupied from pH 4–9, with

Table 3. The modeled protonation and deprotonation reaction constants for the strong and weak sorption sites.

Reactions	$logK_{HMO}$	$logK_{HMO\text{-}2.5Al}$	$logK_{HMO\text{-}5Al}$	$logK_{HMO\text{-}10Al}$
$H^+ + \equiv S^SOH = \equiv S^SOH_2^+$	−4.8	1.6	1.6	1.7
$\equiv S^SOH = \equiv S^SO^- + H^+$	−6.4	−6.1	−5.2	−5.5
$\equiv S^WOH + H^+ = \equiv S^WOH_2^+$	−11.8	−10.2	−3.9	−3.0
$\equiv S^WOH = \equiv S^WO^- + H^+$	−9.9	−9.8	−10.2	−10.2
$\equiv S^SOH + Li^+ = \equiv S^SOLi + H^+$	−3.6	−4.9	−2.8	−4.1
$\equiv S^WOH + Li^+ = \equiv S^WOLi + H^+$	−16.4	−28.4	−22.9	−18.8
$Li^+ + \equiv S^SO^- = \equiv S^SOLi$	−5.0	−6.5	−9.5	−12.4
$Li^+ + \equiv S^SOH_2^+ = \equiv S^SOHLi^+ + H^+$	7.9	1.2	1.3	2.0
$Li^+ + \equiv S^WO^- = \equiv S^WOLi$	0.24	0.37	0.51	0.47
$Li^+ + \equiv S^WOH_2^+ = \equiv S^WOHLi^+ + H^+$	10.1	8.3	0.50	0.62

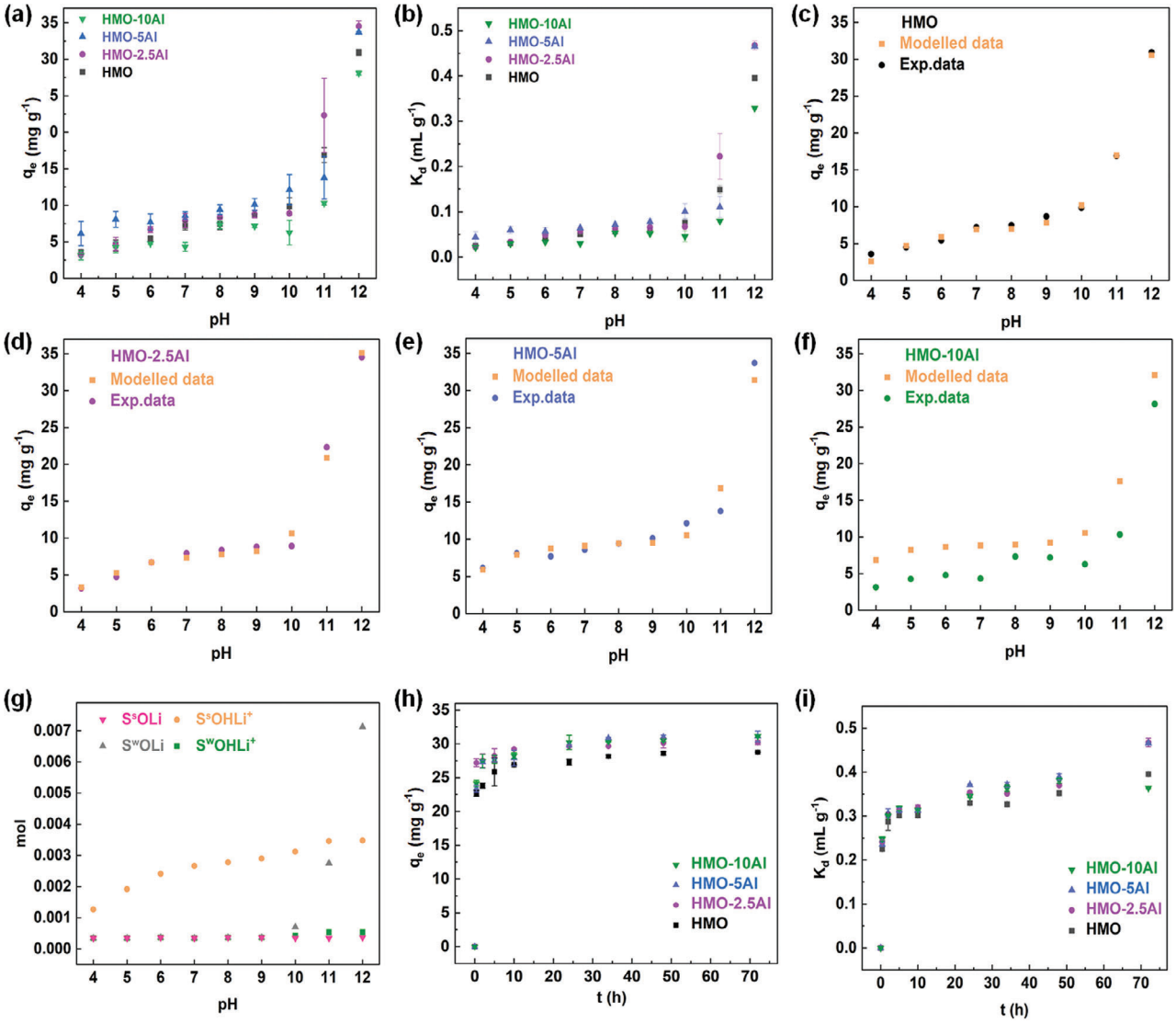

Figure 4. a) The effect of pH on the sorption capacity of HMO and HMO-Al from the equilibrium pH 4 to pH 12; b) The influence of pH on the distribution coefficient; The experimental data and modeling results for the effect of pH from the equilibrium pH 4 to pH 12: c) HMO, d) HMO-2.5Al, e) HMO-5Al, and f) HMO-10Al; g) The modeled moles of adsorbed species on the surface of HMO-2.5Al from pH 4–12; h) The effect of contact time on the Li^+ sorption kinetics of HMO and HMO-Al; i) The influence of contact time on the distribution coefficient.

only a slight increase from pH 10–12. However, above pH 10, vacancy (W) sites began to dominate the sorption process, and the amount of ≡S^{w}OLi increased sharply under high pH conditions.

2.2.3. Sorption Kinetics

The sorption uptake of Li^+ on HMO, HMO-2.5Al, HMO-5Al, and HMO-10Al with an increase in the contact time is illustrated in Figure 4h. A tendency of rapid absorption can be seen within the first 25 min, followed by a gradual increase in the sorption capacity until attaining equilibrium. For HMO-2.5Al, sorption of 27.21 mg g^{-1} was recorded at the time point of 25 min, which was the fastest sorption among the four samples due to its larger surface area and pore size. In addition, HMO-2.5Al possessed the highest distribution coefficient (K_d) value (Figure 4i). Thus, according to the kinetics performance, LMO-2.5Al sorbents exhibit the fastest sorption.

2.2.4. Sorption Isotherms

The effects of the initial Li concentration on the sorption of HMO, HMO-2.5Al, HMO-5Al, and HMO-10Al were investigated in solutions with Li^+ concentrations ranging from 80 to 600 mg L^{-1} at pH 12. According to the results, Li sorption increased with an increase in the initial Li concentration until a plateau was reached at the equilibrium for the four synthesized sorbents (**Figure** 5a). Among these, the highest Li^+ sorption capacity of 35.79 mg g^{-1} was observed for HMO-2.5Al at

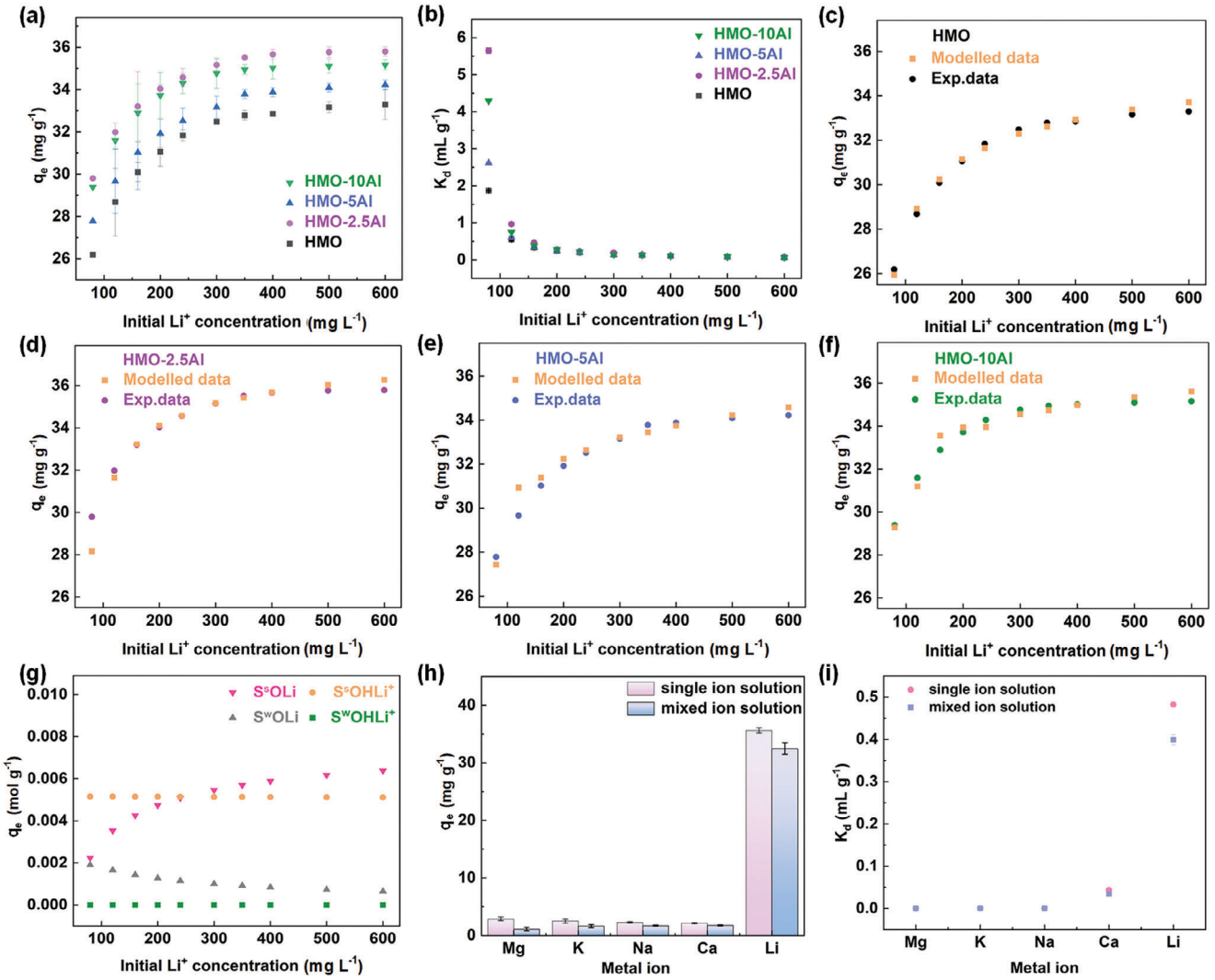

Figure 5. a). The isotherm sorption curves for Li^+ sorption by HMO and HMO-Al; b) Effect of the equilibrium concentration on the selectivity coefficients K_d of HMO and HMO-Al; The experimental and modeled sorption isotherm curves for Li^+ sorption by HMO and HMO-Al: c) HMO, d) HMO-2.5Al, e) HMO-5Al and f) HMO-10Al; g) The modeled moles of adsorbed species on the surface of HMO-2.5 Al in sorption isotherm experiments. Effect of different coexisting ions on the h) Li uptake capacity and i) K_d value of HMO-2.5Al.

an initial Li^+ concentration of 600 mg L^{-1}. Figure 5b illustrates that the K_d values of the four synthesized sorbents decreased with an increase in the Li^+ concentration. The maximum K_d of HMO-2.5 Al was 5.61 mL g^{-1} at an initial Li^+ concentration of 80 mg L^{-1}.

A model was fitted to the sorption isotherm data that considered the surface reactions that occurred on the plane and edge surface sites (S) and vacancies (W) within the structural framework. As can be seen in Figures 5c–f, the model provided a good fit to the sorption isotherm data. The modeled moles of adsorbed species on the surface of HMO-2.5 Al in the sorption isotherm experiments are displayed in Figure 5g. As can be seen, at a low Li concentration (<250 mg L^{-1}), the amount of Li sorbed by the plane and edge (S) sites was higher than that of the vacancy sites (W). With an increase in the Li concentration of the solution, the amount of Li that was sorbed by the vacancy sites increased, and they played a dominant role when the aqueous Li concentration exceeded 300 mg L^{-1}. Thus, we can conclude that, at low Li concentrations, Li sorption preferably occurs at the plane and edge (S) sites, which is easily achieved. Compared with these sites, the diffusion of Li into vacancies requires a higher ionic strength or a longer time to achieve. Thus, the vacancy sites (W) dominate sorption when the plane and edge (S) sites are nearly full.

2.2.5. Effect of Coexisting Ions

The effect of coexisting ions Li^+, Mg^{2+}, K^+, Na^+, and Ca^{2+} in the simulated Li brine solution on Li sorption behavior was investigated with HMO-2.5Al sorption (Table S5, Supporting Information). As illustrated in Figure 5h, the sorption of Li by HMO-2.5Al was higher than that of all other coexisting cations. HMO-2.5Al was found to have the highest K_d value for Li^+ sorption,

Table 4. Relevant selectivity parameters of HMO-2.5Al in the simulation of brine.

	Mg^{2+}	K^+	Na^+	Ca^{2+}	Li^+
C_0 (mg L^{-1})	18271.38	3971.93	5648.53	60.55	158
C_e (mg L^{-1})	18268.32	3968.64	5639.24	51.61	80.37
q_e (mg g^{-1})	1.34	1.45	1.79	1.70	33.17
K_d (mL g^{-1})	0.018	0.091	0.34	36.29	101.54
$\alpha^{Li}{}_M$	6552.76	1327.44	353.08	3.33	-
CF	0.074	0.00036	0.32	28.11	209.98
Ionic radius (Å)	0.72	1.38	1.02	1.00	0.76

indicating the highest selectivity for Li^+ (Figure 5i). The calculated separation factors of $\alpha^{Li}{}_{Ca}$, $\alpha^{Li}{}_{Na}$, $\alpha^{Li}{}_{K}$ and $\alpha^{Li}{}_{Mg}$ were 3.33, 353.08, 1327.44, and 6552.76, respectively, indicating that HMO-2.5Al displays a higher priority for Li sorption (**Table 4**). The calculated *CF* of Li^+ was much higher than that of the other cations, indicating that the interference from other cations in the process of Li^+ sorption by HMO-2.5Al was very low. Li^+ has the smallest ionic diameter of 0.076 nm, which is preferred over larger cations such as Na^+ (0.102 nm) and K^+ (0.138 nm) (Table 4). Although Mg^{2+} has a similar ionic diameter of 0.072 nm, compared with Li^+, its extremely low sorption by the sorbent demonstrates that more energy is needed to enter the lattice of the ion sieve.[52] In summary, HMO-2.5Al possesses the highest selectivity for Li^+ sorption among all other cations tested.

2.2.6. Cyclic Stability Performance

To evaluate the stability of the prepared HMO and HMO-2.5Al sorbents in the sorption and desorption processes, the sorption capacity and dissolution loss of Mn were investigated by repeating five sorption–desorption cycles. For the first cycle, the lithium sorption capacity of HMO and HMO-2.5Al was 42.60 and 44.49 mg g^{-1}, respectively. By the fifth cycle, the sorption capacities had decreased to 31.35 mg g^{-1} for HMO and 36.23 mg g^{-1} for HMO-2.5Al (**Figure 6**a,b). Additionally, regarding the loss rate of Mn through dissolution, after the fifth cycle, the Mn loss rates in the sorption process were less than 0.2%, which is negligible. However, Mn loss rates in the desorption process were 5.01% for HMO and 4.53% for HMO-2.5Al. The lower Mn dissolution of HMO-2.5Al is attributed to the doping of magnesium ions, which decreases the amount of Mn^{3+}. Additionally, the substitution of Mn^{3+} with Al^{3+} inhibits the disproportionation reaction of Mn. Above all, all results demonstrate that the sorbent HMO-2.5Al possesses a higher Li sorption capacity and lower Mn loss rate, which results from Al doping of the HMO material. After five sorption–desorption cycles, the dried HMO and HMO-2.5Al were analyzed by XRD (Figure 6e,f). Compared with the pristine LMO and HMO, all the XRD peaks after five sorption–desorption cycles indicated high stability.

The Mn-type sorbents examined in previously published research have been listed in **Table 5**. Compared with these, the synthesized HMO material of this study displayed a higher sorption capacity of 42.6 mg g^{-1} at a concentration of 150 mg L^{-1} Li^+. This higher capacity was due to our novel synthesis process, adding $LiNO_3$ during the synthesis of HMO. Undoubtedly, HMO-2.5Al possesses an even higher capacity with Al doping, suggesting that doping of HMO with Al can reduce manganese loss and enhance the Li sorption capacity.

2.2.7. Sorption Mechanism

For insights into the mechanism of Li sorption on synthesized Mn-type sorbents, XRD, Raman spectroscopy, and XPS were

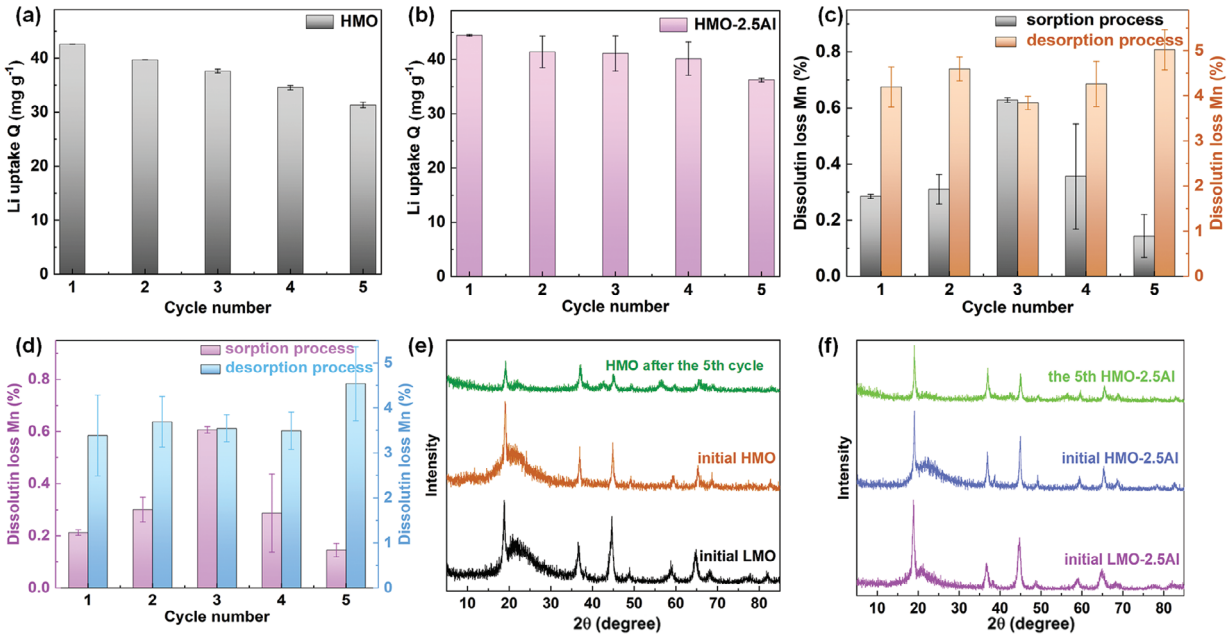

Figure 6. The sorption capacity of a) HMO and b) HMO-2.5Al; Dissolution loss R of c) HMO and d) HMO-2.5Al in the desorption process and sorption process over five cycles; e) XRD patterns of LMO and (f) LMO-2.5Al before and after desorption after the fifth cycle.

Table 5. Comparison of the sorption capacity in the present study with previous research.

Adsorbent	Solution	C_{Li^+} (mg L^{-1})	q_e (mg g^{-1})	Refs.
$H_{1.6}Mn_{1.6}O_4$-Zr-2.4%	Salt Lake	150	25.96	[16]
$Li_{1.6}Mg_xMn_{1.6-x}O_4$	LiOH	156	35.6	[26]
HMO-Al-5%	LiCl	167	29.9	[27]
$LiMn_{2-x}Fe_xO_4$	LiCl	200	34.8	[30]
$LiAl_xMn_{2-x}O_4$	LiOH	50	27.66	[29]
$Li_{1.6}Mn_{1.6}O_4$	Salt Lake	266	27.15	[53]
$Li_{1.6}Mn_{1.6-x}Cr_xO_4$	Salt Lake	222	31.67	[48]
HMO/Al_2O_3	Seawater	30	6.2	[54]
$H_{1.6}Mn_{1.6}O_4$/PAN	LiCl/LiOH	35	10.3	[22]
LMO-Na	LiCl	167	33.5	[55]
HMO	LiOH	150	42.60	This study
HMO-Al-2.5%	LiOH	150	44.49	This study

conducted on the sorbents before and after sorption. The XRD pattern revealed no significant shifts in the peak positions of the materials before and after sorption, suggesting that their chemical structure remained stable throughout the process (**Figure** 7a). The vibration features of the Raman spectrum of LMO-2.5Al showed a new peak located at ≈365 cm^{-1} (Figure 7b), which can be attributed to the vibration frequency of LiO_6 octahedra, indicating that Li successfully intercalated in HMO-2.5Al.[56] The shift of Mn–O symmetric stretching vibration at 643.59 cm^{-1} for HMO-2.5Al to 640.67 cm^{-1} for LMO-2.5Al is attributed to the weak vibration of the MnO_6 structure in the bonding and force constants upon Li intercalation.[57] The XPS spectra of the Mn2p3 orbit, Li1s, and O1s were recorded. The Li1s XPS spectra were observed after Li sorption on sorbents from 54–55 eV binding energy (Figure 7c). Additionally, we observed a slight decrease of ≈2% in the Mn^{4+}: Mn^{3+} ratio, with an Mn loss rate of less than 0.2% for HMO and HMO-2.5 Al after 5 cycles in the sorption process, which may be considered a negligible effect on the sorbent (Figure 7d). Moreover, a slight shift in the O1s peak from ≈529.6 to ∼530.0 eV was observed (Figure 7e), along with a 13% decrease in the ratio of -OH groups compared to the pristine sorbent (Figure 7f). This suggests that -OH groups were involved in the Li sorption process, probably through a surface ion-exchange or surface complexation reaction during Li extraction.

Based on the batch experiment, surface complexation and ion-exchange modeling, and the calculated formula, a two-stage sorption mechanism is proposed (Figure 7g). Apparently, at least two physical sorption sites exist on LMO-type material surfaces: plane and edge surface sites (S) and vacancies (W) in the structural framework. From the sorption mechanism based on these analyses, it can be concluded that at low Li concentrations, Li sorption preferentially occurs at the plane and edge (S) sites, which is readily facilitated through surface ion-exchange reactions. In contrast, the diffusion of Li into vacancy sites requires a higher ionic strength or an extended time to proceed as a surface complexation reaction. Accordingly, the proposed mechanism encompasses two distinct sorption stages at pH ≥ 12: surface ion-exchange reactions in stage I, Equations (8) and (11),

$$Li^+ + \equiv S^wOH_2^+ \Leftrightarrow \equiv S^wOHLi^+ + H^+ \quad (11)$$

and surface complexation reactions in stage II, Equations (10) and (12),

$$\equiv S^WOH \Leftrightarrow \equiv S^WO^- + H^+ \quad (12)$$

The surface ion-exchange reactions first occur between the Li^+ in the solution and S sites. When the S sites approach saturation, the vacancy sites become the dominant sorption sites through surface complexation reactions. In other words, for the four synthesized sorbents at pH 12, a higher vacancy rate leads to a greater sorption capacity. The experimental results confirm the proposed mechanism: HMnO-2.5Al, which had the highest number of vacancies among the four synthesized sorbents, exhibited the greatest capacity for Li sorption.

3. Conclusion

This study provides novel insights into Li sorption mechanisms by systematically investigating the structure, surface, and defect vacancies of synthesized LiMnO and Al-doped LiMnO sorbents. Through characterizations such as XRD, FTIR, Raman spectroscopy, TG, XPS and ICP-AES, the formulas and vacancy ratios of synthesized LiMnO and Al-doped LiMnO sorbents were determined. Among the sorbents, HMnO-2.5Al demonstrated superior performance, achieving a Li^+ sorption capacity of 44.49 mg g^{-1} and reducing the Mn loss to 3.38%. Its high selectivity for lithium was evident from exceptional separation factors, including α^{Li}_{Mg} at 6552.76.

A two-stage sorption mechanism was elucidated, with planar and edge surface sites dominating at lower pH and Li^+ concentrations and vacancy sites taking precedence at higher pH and Li^+ levels. The role of pH in facilitating lithium-ion diffusion to vacancy sites was highlighted, aligning with the observed superior performance of HMnO-2.5Al, which possessed the highest vacancy density. Additionally, the desorption process was proposed to involve surface ion-exchange reactions.

These findings demonstrate that HMnO-2.5Al, with its high selectivity, capacity, and durability, offers significant potential for application in the direct lithium extraction industry, advancing both understanding and practice in this field.

4. Experimental Section

Materials and Chemicals: Sodium hydroxide (NaOH, 96%), nitric acid (HNO_3, 65–68%), hydrochloric acid (HCl, 36–38%), sodium nitrate ($NaNO_3$, 99%), magnesium chloride hexahydrate ($MgCl_2{\cdot}6H_2O$, 98%), potassium chloride (KCl, 99.8%), sodium chloride (NaCl, 99%), calcium chloride ($CaCl_2$, 96%), and aluminum nitrate hydrate ($Al(NO_3)_3{\cdot}9H_2O$, 99%) were purchased from Sinopharm Chemical Reagent. Lithium hydroxide monohydrate ($LiOH{\cdot}H_2O$, 99%), manganese oxide (Mn_2O_3, 98%), and lithium nitrate ($LiNO_3$, 99%) were purchased from Aladdin. All chemical reagents were used as received without further purification. Milli-Q water with a resistivity of >18.5 MΩ was used in all the experiments.

Synthesis—Synthesis of $LiMnO_2$: $LiMnO_2$ was synthesized by improving the method reported by Chitrakar.[58] First, $LiOH{\cdot}H_2O$ and Mn_2O_3 powders were dissolved in deionized water, with the molar ratio of Li: Mn being 9. After mixing in the homogeneous phase, the liquid was transferred to an autoclave for hydrothermal reaction at 120 °C for 1 day. The filtration used deionized water and drying at 60 °C. Finally, the black powder obtained was the manganese-based lithium-ion sieve precursor $LiMnO_2$.

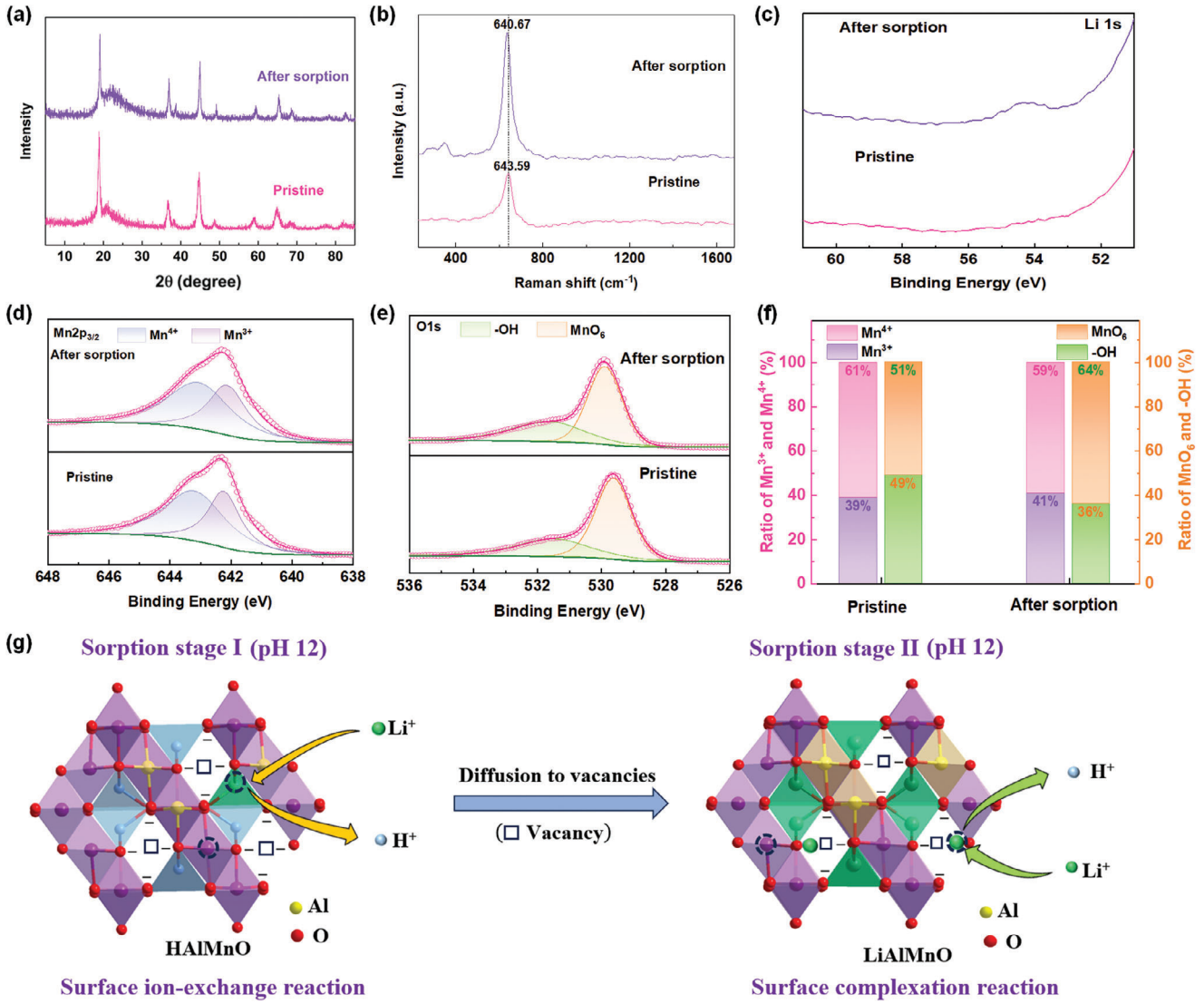

Figure 7. The characterization of HMO-2.5 Al in the pristine form and after 5 cycles of Li sorption: a) XRD, b) Raman spectra, c) XPS Li1s, d) XPS $Mn2P_{3/2}$, e) XPS O1s, and f) the transfer of Mn^{4+}/Mn^{3+} and MnO_6/-OH; g) The proposed two-stage mechanism for direct lithium extraction using Al-doped LMO at pH ~12.

Synthesis—Synthesis of Al-Doped LiMnO Materials: Al-doped LiMnO was synthesized by mixing $LiNO_3$ solution with the obtained $LiMnO_2$ powder at a Li: Mn molar ratio of 1:10. Subsequently, $Al(NO_3)_3$ solution (pH 12) was added to the mixed solution in varying molar ratios of Al to Mn, specifically 0%, 2.5%, 5%, and 10%. The reaction of all mixed solutions occurred under ultrasonic stirring for 2 h at 60 °C. After filtration, washing with deionized water, and drying in an oven, the resulting solid was placed in a tube furnace for calcining at 400 °C for 4 h with air flow. Finally, brown powders with different molar ratios of Al to Mn (0%, 2.5%, 5%, and 10%) were obtained. These samples were referred to as LMO, LMO-2.5Al, LMO-5Al, and LMO-10Al, respectively, in the following sections.

Synthesis—Synthesis of H-Type HMO and HMO-Al: H-type HMO and HMO-Al were prepared with an acid reaction method using nitric acid, with 1.0 g of LMO, LMO-2.5Al, LMO-5Al, and LMO-10Al each being placed in 400 mL of 0.1 mol L^{-1} HNO_3 solution and stirred at 500 rpm for 24 h at room temperature to reach equilibrium. Subsequently, after phase separation, the resulting solid was washed with deionized water and dried in an oven at 60 °C for 24 h. Finally, the HMO, HMO-2.5Al, HMO-5Al, and HMO-10Al materials were obtained. To determine the chemical composition of the samples, 50 mg of each sample was added to 10 mL of aqua regia solution (a mixture of HCl and HNO_3, volume ratio = 3:1).[29] The supernatants were collected after complete dissolution and were then filtered using a syringe PTFE membrane filter with a pore size of 0.2 µm. The obtained filtrates were used for ICP-AES analysis.

Batch Sorption Experiments—Potentiometric Titration: The direct titration was performed using the synthesized HMO, HMO-2.5Al, HMO-5Al, and HMO-10Al in a batch manner. Fifty milligrams of each sample were mixed with 19 mL of 1 M $LiNO_3$ solution and equilibrated at a stirring speed of 60 rpm for 24 h. The equilibrium pH of the samples was recorded, followed by the addition of varying volumes (0–500 µL) of 1 M LiOH solution. After this, all the samples were further equilibrated for another 24 h, followed by pH measurement.

Batch Sorption Experiments—Effect of pH: The effect of pH on the Li sorption capacity at equilibrium was examined by adjusting the pH of the Li^+ solution using NaOH or HNO_3 solutions. Typically, 50 mg of HMO, HMO-2.5Al, HMO-5Al, and HMO-10Al materials were placed in 20 mL of

the Li^+ solution with an initial concentration of 150 mg L^{-1}. The mixed samples and solutions were equilibrated at a stirring speed of 60 rpm for 72 h at room temperature. After phase separation, the pH of the supernatant solution was measured. The lithium sorption capacity (q_e, mg g^{-1}) and the distribution coefficient (K_d, mL g^{-1}) were calculated according to Equations (13) and (14):[59]

$$q_e = (C_0 - C_e)\, V/m \tag{13}$$

$$K_d = (C_0 - C_e) \times V/\,(m \times C_e) \tag{14}$$

where C_0 and C_e are the initial and residual lithium-ion concentrations (mg L^{-1}), V is the volume of the solution (L), and m is the mass of the adsorbent (g).

Batch Sorption Experiments—Kinetics Study and Isotherm Sorption: The sorption kinetics were studied at specific time intervals (from 25 min to 72 h). Fifty milligrams of HMO, HMO-2.5Al, HMO-5Al, and HMO-10Al materials were placed in 20 mL of the Li^+ solution with an initial concentration of 150 mg L^{-1} at pH 12. The sorption isotherms were obtained by shaking the mixture, having concentrations of 80–600 mg L^{-1} with an adequate interval, for 72 h at room temperature. For all obtained samples, after phase separation, the Li concentrations of the supernatants were analyzed by ICP-AES. The amount of Li^+ adsorbed at a given time (q_t) can be calculated using Equation (15) and plotted against the contact time (t) to generate the adsorption kinetics curve at various temperatures.

$$q_t = (C_{0-}C_t)\, V/m \tag{15}$$

Batch Sorption Experiments—Effect of Coexisting Ions: To assess the selectivity of the sorption behavior for the prepared adsorbents, experiments were conducted in simulated lake brine with a Li concentration of 155 mg L^{-1}, Mg concentration of 10 523 mg L^{-1}, K concentration of 3630 mg L^{-1}, Na concentration of 5390 mg L^{-1}, and Ca concentration of 72 mg L^{-1}. Fifty milligrams of HMO-2.5Al were placed into 20 mL of the above simulated lake brine in a rotary mixer (60 rpm) for 24 h. The concentration factor (*CF*) and separation factor (α) of different metal ions in a multi-component system were determined using Equations (16) and (17) respectively:[16,60]

$$CF = q_e/C_0 \tag{16}$$

$$\alpha^{Li}{}_M = K^{Li}{}_d/K_d{}^M \tag{17}$$

$\alpha^{Li}{}_M$ was used to analyze the degree of separation of Li^+ from other metal ions, while *CF* was indicative of the influence of interfering ions on the sorption of target ions by HMO-2.5Al.

Batch Sorption Experiments—Cyclic Stability Performance: The reusability of HMO and HMO-2.5Al was evaluated through five consecutive sorption–desorption cycles. In each cycle, for the sorption experiments, 1.0 g of HMO and HMO-2.5Al were introduced into separate 400 mL volumes of 0.05 M LiOH solution for a 72-h equilibrium period. For the desorption experiments, the Li-loaded HMO and HMO-2.5Al were placed in a 0.5 M HNO_3 solution to release the adsorbed lithium.

Modeling Methods: The results for the titration, pH effect (sorption edge), and sorption isotherm experiments were modeled with a programming code that coupled PHREEQC and Python. PHREEQC was a geochemical modeling tool that can perform various geochemical calculations, e.g., speciation calculations, ion exchange and surface complexation reactions, and transport calculations. The PHREEQC codes were fitted into Python script through the iphreeqc tool, which was a COM version of PHREEQC for coupling purposes with all PHREEQC capabilities. Python was a popular computer programming language that was widely used in scientific calculations. In this study, Python was used for control of the fitting iterations, optimization, and visualization of the modeling results. All the calculations were performed based on the standard phreeqc.dat database, because Li data were well documented in the database.

Two types of sorption sites were assumed in all the modeling processes, termed the S sorption site ($\equiv S^SOH$) and W sorption site ($\equiv S^WOH$). The assumption of two sorption sites was based on the structural characteristics of LMO-type materials, which suggest the existence of at least two types of physical sorption sites: planar and edge surface sites (S) and vacancies (W) within the structural framework. Both surface complexation reactions and ion exchange reactions were assumed to occur between Li species and assumed surface sites.

Model development was performed by fitting titration data, pH effect data, and sorption isotherm data in iterative processes. The titration data were modeled first to provide basic information on the protonation and deprotonation reactions of $\equiv S^SOH$ and $\equiv S^WOH$ sites, i.e., the interactions between surface sites and H^+ or Li^+ in the aqueous phase. The modeled *logK* values (equilibrium constants) of protonation and deprotonation reactions were kept constant in all the modeling processes. Modeling of the sorption edge and sorption isotherm results was performed by fitting the assumed reactions to both $\equiv S^SOH$ and $\equiv S^WOH$ sites. The modeling process was iterated until a group of parameters was identified that could provide a good description of all the titration, sorption edge, and sorption isotherm experimental data. The optimization between the experimental and modeled data was performed by minimizing the squares of the difference between them (least square errors). The absolute errors between iterations that were acceptable for convergence were set to be 10^{-7}.

Characterization: XRD patterns were recorded using a MiniFlex600 X-ray powder diffractometer with the setting of 40 kV, 40 mA, and Cu-Kα radiation. The synthesized samples were imaged via FESEM (SU-8010, Tokyo, Japan) and HRTEM (JEM-F200, Japan). A FTIR (Bruker Optics, Germany) was used to analyze the surface functional groups of the synthesized LMO and LMO-Al at ≈298 K over the range of 4000–600 cm^{-1}. The Raman spectra were recorded on a LabRaM HR800 microscope equipped with a 24 mW He–Ne green laser (532 nm) operating at 0.24 mW. TGA was performed using a Mettler Toledo TGA850 with a heating rate of 10 °C min^{-1} in N_2 flow. The specific surface area, pore volume, and pore-size distribution of the synthesized samples were measured by N_2 physisorption at 77 K with a BET (ASAP2020C, American Micromeritics). The concentrations of Li ions and other ions were measured using a Perkin Elmer Avio200 ICP-AES. An XPS (Thermo Fisher ESCALAB 250xi) equipped with REELS, ISS, SPS, and a hemispherical electron analyzer was used to analyze the surface properties of the synthesized samples and the samples after sorption.

Supporting Information

Supporting Information is available from the Wiley Online Library or from the author.

Acknowledgements

S.Y. and S.P. contributed equally to this work. The research leading to these results received funding from the Chinese Academy of Sciences Pioneer "Hundred Talents Program" Young Talents (Class C) and the project "Brines of RIS countries as a source of CRM and energy supply–BrineRIS" under grant agreement no. 19116 from EIT RawMaterials. This publication reflects only the authors' views, exempting the Community from any liability. The authors would like to thank Prof. Hongli Bao for her support.

Conflict of Interest

The authors declare no conflict of interest.

Data Availability Statement

The data that support the findings of this study are available from the corresponding author upon reasonable request.

Keywords

Al-doped manganese dioxide sieves, direct lithium extraction, modeling, mechanism

Received: November 16, 2024
Revised: January 20, 2025
Published online:

[1] D. Weng, H. Duan, Y. Hou, J. Huo, L. Chen, F. Zhang, J. Wang, *Prog. Nat. Sci.: Mater. Int.* **2020**, *30*, 139.
[2] Y. Yang, H. Jiang, J. Yu, *Sep. Purif. Technol.* **2022**, *281*, 119596.
[3] P. Xu, J. Hong, X. Qian, Z. Xu, H. Xia, X. Tao, Z. Xu, Q.-Q. Ni, *J. Mater. Sci.* **2021**, *56*, 16.
[4] X. Guo, S. Hu, C. Wang, H. Duan, X. Xiang, *Ind. Eng. Chem. Res.* **2018**, *57*, 6618.
[5] S. Hu, Y. Sun, M. Pu, R. Yun, X. Xiang, *Sep. Purif. Technol.* **2019**, *229*, 115813.
[6] Z. Zhang, J. Tang, M. Su, J. Xu, K. Shih, *ACS Sustainable Chem. Eng.* **2023**, *11*, 16124.
[7] D. Gao, X. Yu, Y. Guo, S. Wang, M. Liu, T. Deng, Y. Chen, N. Belzile, *Chem. Res. Chin. Univ.* **2015**, *31*, 621.
[8] T. H. Nguyen, M. S. Lee, *Processes* **2018**, *6*, 55.
[9] Y. Zhang, L. Wang, W. Sun, Y. Hu, H. Tang, *J. Ind. Eng. Chem.* **2020**, *81*, 7.
[10] B. Haruna, Z. Luo, M. Aminu, J. Kuva, R. Koivula, H. J. X. u Bao, *Batteries* **2024**, *10*, 254.
[11] H. Yu, G. Naidu, C. Zhang, C. Wang, A. Razmjou, D. S. Han, T. He, H. Shon, *Desalination* **2022**, *539*, 115951.
[12] J. Farahbakhsh, F. Arshadi, Z. Mofidi, M. Mohseni-Dargah, C. Kök, M. Assefi, A. Soozanipour, M. Zargar, M. Asadnia, *Desalination* **2024**, *575*, 117249.
[13] E. W. Wiikinkoski, J. Xu, W. Zhang, S. Hietala, R. T. Koivula, *ChemistrySelect* **2018**, *3*, 9583.
[14] J. Xu, E. Wiikinkoski, R. Koivula, W. Zhang, B. Ebin, R. Harjula, *J. of Sustain. Metall.* **2017**, *3*, 646.
[15] J. Xu, R. Koivula, W. Zhang, E. Wiikinkoski, S. Hietala, R. Harjula, *Hydrometallurgy* **2018**, *175*, 170.
[16] L. Wang, J. Wang, X. Wang, *Sep. Purif. Technol.* **2022**, *303*, 121933.
[17] Q.-H. Zhang, S.-P. Li, S.-Y. Sun, X.-S. Yin, J.-G. Yu, *Chem. Eng. Sci.* **2010**, *65*, 169.
[18] S. Choi, G. Hwang, S. Ilyas, Y. Han, N. V. Myung, B.-c. Lee, Y. Song, H. Kim, *Sep. Purif. Technol.* **2020**, *242*, 116757.
[19] H.-J. Hong, I.-S. Park, T. Ryu, J. Ryu, B.-G. Kim, K.-S. Chung, *Chem. Eng. J.* **2013**, *234*, 16.
[20] L. Liu, Q. Kuang, S. Xu, W. Pan, Y. Liu, J. Zhou, A. Tang, J. Xue, *J. Mol. Liq.* **2023**, *380*, 121780.
[21] Q. Wang, X. Du, F. Gao, F. Liu, M. Liu, X. Hao, K. Tang, G. Guan, A. Abudula, *Sep. Purif. Technol.* **2019**, *226*, 59.
[22] G. Zhang, C. Hai, Y. Zhou, W. Tang, J. Zeng, Y. Liu, S. Dong, G. Peng, *Chem. Eng. J.* **2022**, *450*, 137912.
[23] Y. Zhang, H. Xing, Q. Meng, Q. Liu, H. Liu, L. Ynag, *Sep. and Purif. Technol.* **2024**, *348*, 127739.
[24] G. Zhang, J. Zhang, Y. Zhou, G. Qi, Y. Wu, C. Hai, W. Tang, *Colloids Surf. A: Physicochem. Eng. Asp.* **2019**, *583*, 12395.
[25] J. Alonso, M. Martinez-Lope, M. Casais, M. Fernández-Díaz, *Inorg. Chem.* **2000**, *39*, 917.
[26] L. Bao, J. Zhang, J. Wu, G. Zhang, Y. Yang, W. Tang, M. Xue, *Hydrometallurgy* **2022**, *209*, 105772.
[27] F. Qian, M. Guo, Z. Qian, B. Zhao, J. Li, Z. Wu, Z. Liu, *Sep. and Purif. Technol.* **2021**, *264*, 118433.
[28] F. Qian, B. Zhao, M. Guo, Z. Qian, N. Xu, Z. Wu, Z. Liu, *Hydrometallurgy* **2020**, *193*, 105291.
[29] M. Chen, R. Wu, S. Ju, X. Zhang, F. Xue, W. Xing, *Microporous Mesoporous Mater.* **2018**, *261*, 29.
[30] J.-m. Gao, Z. Du, Q. Zhao, Y. Guo, F. Cheng, *J. Mater. Res. Technol.* **2021**, *13*, 228.
[31] J. C. Hunter, *J. Solid State Chem.* **1981**, *39*, 142.
[32] X.-M. Shen, A. Clearfield, *J. Solid State Chem.* **1986**, *64*, 270.
[33] B. Deng, H. Nakamura, Q. Zhang, M. Yoshio, Y. Xia, *Electrochim. Acta* **2004**, *49*, 1823.
[34] J. Hao, H. Bai, J. Liu, F. Yang, Q. Li, C. Su, J. Guo, *J. Alloys Compd.* **2016**, *668*, 200.
[35] W. Hao, Y. Xiyun, Y. Zhoulan, C. Gai-Fang, X. Hui, *Chin. J. of Inorg. Chem.* **2017**, *33*, 1775.
[36] H. Wang, Y.-n. Wang, Y. Sun, X. Pan, D. Zhang, Y. F. Tsang, *Process Saf. Environ. Prot.* **2018**, *113*, 40.
[37] Y.-M. Hon, H. Chung, K.-Z. Fung, M.-H. Hon, *J. Solid State Chem.* **2001**, *160*, 368.
[38] S. Ye, J. Bo, C. Li, J. Cao, Q. Sun, Y. Wang, *Electrochim. Acta* **2010**, *55*, 2972.
[39] M. Helan, L. J. Berchmans, T. P. Jose, A. Visuvasam, S. Angappan, *Mater. Chem. Phys.* **2010**, *124*, 439.
[40] M. D. Pedowitz, S. Kim, D. I. Lewis, B. Uppalapati, D. Khan, F. Bayram, G. Koley, K. M. Daniels, *J. Microelectromech. Syst.* **2020**, *29*, 846.
[41] C. Julien, M. Massot, R. Baddour-Hadjean, S. Franger, S. Bach, J. J. S. S. I. Pereira-Ramos, *Solid State Ionics* **2003**, *159*, 345.
[42] Q. Feng, Y. Miyai, H. Kanoh, K. Ooi, *Langmuir* **1992**, *8*, 1861.
[43] Y. Zhang, X. Li, X. Chen, R. Koivula, J. Xu, *J. Hazard. Mater.* **2022**, *425*, 127957.
[44] C.-M. Yoon, J. Ryu, J. Yun, Y. K. Kim, J. Jang, *ACS Appl. Mater. Interfaces* **2018**,*10*, 6570.
[45] F.-X. Bu, M. Hu, W. Zhang, Q. Meng, L. Xu, D.-M. Jiang, J.-S. Jiang, *Chem. Comm.* **2015**, *51*, 17568.
[46] G. Zhang, J. Zhang, J. Zeng, Y. Sun, Y. Shen, X. Li, X. Ren, C. Hai, Y. Zhou, W. Tang, *Colloids Surf. A: Physicochem. Eng. Asp.* **2021**, *629*, 127465.
[47] L. Shao, A. Sun, Y. Zhang, L. Yu, N. Suo, Z. Zuo, *J. Mater. Sci.: Mater. Electron.* **2021**, *32*, 20474.
[48] G. Cao, X. Yang, Z. Yin, Y. Lei, H. Wang, J. Li, *Bull. Chem. Soc. Jpn.* **2019**, *92*, 1205.
[49] L. Wang, Y. Zhang, X. Li, C. He, M. Szlachta, Y. Chen, J. Xu, *Sep. and Purif. Technol.* **2024**, *346*, 127497.
[50] C. Nong, X. Li, R. Koivula, J. Xu, M. Szlachta, *Chem. Eng. J.* **2023**, *477*, 147134.
[51] M. J. Iqbal, Z. Ahmad, *J. Power Sources* **2008**, *179*, 763.
[52] L. A. Limjuco, G. M. Nisola, C. P. Lawagon, S.-P. Lee, J. G. Seo, H. Kim, W.-J. Chung, *Colloids Surf. A: Physicochem. Eng. Asp.* **2016**, *504*, 267.
[53] X. Shi, D. Zhou, Z. Zhang, L. Yu, H. Xu, B. Chen, X. Yang, *Hydrometallurgy* **2011**, *110*, 99.
[54] H.-J. Hong, I.-S. Park, T. Ryu, B.-G. Kim, K.-S. Chung, *Ind. Eng. Chem. Res.* **2019**, *58*, 8342.
[55] F. Qian, B. Zhao, M. Guo, Z. Wu, W. Zhou, Z. Liu, *Sep. and Purif. Technol.* **2021**, *256*, 117583.
[56] C. Julien, A. Rougier, E. Haro-Poniatowski, G. Nazri, *Section A. Mol. Cryst. Liq. Cryst.* **1998**, *311*, 81.
[57] C. Julien, M. Massot, R. Baddour-Hadjean, S. Franger, S. Bach, J. Pereira-Ramos, *Solid State Ionics* **2003**, *159*, 345.
[58] R. Chitrakar, K. Sakane, A. Umeno, S. Kasaishi, N. Takagi, K. Ooi, *J. Solid State Chem.* **2002**, *169*, 66.
[59] D. Ding, K. Li, D. Fang, X. Ye, Y. Hu, X. Tan, H. Liu, Z. Wu, *ChemistrySelect* **2019**, *4*, 13630.
[60] N. Linneen, R. Bhave, D. Woerner, *Sep. and purif. technol.* **2019**, *214*, 168.